Nanoparticle-stabilized Microemulsions for Enhanced Oil Recovery from Heterogeneous Rocks

Tianzhu Qin,[1] Lamia Goual,[1]* Mohammad Piri,[1] Zhongliang Hu,[2] Dongsheng Wen[2]

1. Department of Petroleum Engineering, University of Wyoming, Laramie, WY 82071, USA

2. Department of Chemical and Process Engineering, University of Leeds, Leeds, LS2 9JT, UK

* Email: lgoual@uwyo.edu, phone: 307-766-3278

ABSTRACT

Surfactant-stabilized microemulsions (MEs) are often used to reduce the capillary forces responsible for trapping residual non-aqueous phase liquids (NAPLs) such as crude oils inside subsurface geological formations. Recent studies showed that the presence of nanoparticles (NPs) in the ME phase could enhance NAPL recovery, however their interfacial interactions and the impact of rock characteristics (e.g., mineralogy, topology, etc.) is still unclear, especially at the microscale. The objective of this study was to understand the effect of microemulsions stabilized by nanoparticles (MENP) on pore-scale fluid displacement mechanisms in a heterogeneous aquifer rock such as Arkose sandstone. A novel method was developed to synthesize silicon oxide (SiO_2) *in-situ* in a ME. These nanoparticles had less tendency to agglomerate compared to nanopowders and promoted the formation of pickering emulsions. The impact of ME and MENP on NAPL displacement in Arkose was examined using a micro-CT scanner integrated with a miniature core flooding system. NAPL-aged cores were subjected to flooding tests with different aqueous solutions (brine, ME, and MENP) to investigate the effectiveness of these additives in enhancing NAPL removal. We found that ME promoted NAPL mobilization by reducing IFT and enhancing emulsification. The ability of ME to solubilize adsorbed NAPL layers contributed to a wettability alteration from NAPL-wet to weakly water-wet. Therefore, ME could remove 20% of additional NAPL after waterflooding. The incremental NAPL removal with MENP (34.3%) was higher than that of ME due to the emulsification of

NAPL into even smaller droplets where NPs and surfactants synergistically interacted at the interface. The small NAPL droplets could penetrate small capillary elements of the rock that were inaccessible to ME, leading to stronger wettability alteration especially in microporous carbonate cements.

Keywords: Microemulsion, NAPL, Crude oil, Nanoparticle, Heterogeneous rock, Enhanced oil recovery, Mobilization, Solubilization

1. INTRODUCTION

Understanding multi-phase flow processes is critical for the remediation of contaminated aquifers and enhanced oil recovery (EOR). In subsurface geological formations, non-aqueous phase liquids (NAPLs) such as crude oils are often entrapped in the form of ganglia within the pores due to the large capillary forces across the interface between NAPL and brine phases.[1] These forces give rise to a capillary pressure that is a function of pore geometry, interfacial tension (IFT) between the two fluids, and rock wettability, often quantified by the contact angle (CA) that a fluid drop creates on its surface.[1] The wettability of pore surfaces is dependent on the properties of rocks and NAPLs. Surface-active asphaltene and resin molecules present in NAPLs tend to adsorb on mineral surfaces, form an organic layer, thereby altering their wettability from water-wet to neutral- or oil-wet.[2,3] The extent to which wettability is altered is variable due to mineral heterogeneities in subsurface formations, making the wetting preference of rock surfaces difficult to describe.

Capillary forces can be reduced by the addition of appropriate surfactant formulations. Surfactants are organic molecules that contain both hydrophobic groups (i.e., tails) and hydrophilic groups (i.e., heads).[4] This structure makes them energetically favorable to adsorb on oil/water interfaces, decrease the IFT, and consequently mobilize small NAPL droplets through porous media.[4,5] On the other hand, the propensity of surfactant molecules to self-assemble above their critical micelle concentration (CMC) enables them to

solubilize adsorbed NAPL and restore the wettability of pore surfaces from neutral- or NAPL-wet back to water-wet.[6,7] The performance of surfactants can be further enhanced by putting them into micro-emulsified state.[8,9] Microemulsions (MEs) are composed of water, hydrocarbon, and amphiphiles, which are optically isotropic and thermodynamically stable liquid solutions.[10] They differ from ordinary emulsions in that they can be prepared with little or no input of mechanical energy.[11] The oil phase, also called carrier fluid, could be a terpene solvent such as d-limonene.[12] Various water-soluble surfactants with hydrophile-lipophile balance (HLB) between 8 and 18 have been applied as emulsifiers; examples are linear alcohol ethoxylates and alkylpolyglucosides.[12–15] Co-surfactants on the other hand often consist of short or medium chain alcohols such as 2-propanol.[13,14,16] These formulations are able to carry surfactant molecules deep into the formation and minimize losses due to adsorption on rock surfaces. Additionally, d-limonene can penetrate adsorbed NAPL layers and reduce their interaction with minerals.[17] With their unique ability to swell these layers, MEs usually provide more effective NAPL solubilization than surfactants, especially in rocks containing carbonate cements.[8,9]

Recent studies showed that nanoparticles (NPs) could be used as stabilizers for MEs under harsh subsurface conditions, such as high temperature and salinity.[18] Nanoparticles are particles between 1 and 100 nanometers in size,[19] that tend to adsorb at oil/water interfaces to form pickering emulsions. The steric forces formed by NPs, especially in the presence of surfactants, provide a mechanical barrier against coalescence and thermal fluctuations, such as lamella drainage and hole formation, thereby enhancing emulsion stability.[20–23] Various types of NPs have been utilized to stabilize MEs. Examples are clays, iron oxide (Fe_2O_3), super/paramagnetic, partially hydrophobic and hydrophilic SiO_2 NPs.[24–29] These NP-stabilized MEs were often prepared by a two-step method. NPs are initially synthesized using physical or chemical methods then the nano-sized powder particles are dispersed in base fluids, such as brine.[30–32] This method requires NPs to be synthesized and stored prior to the preparation of MEs, therefore leading to additional cost and agglomeration tendency.[29] This problem can be solved by preparing NP–stabilized MEs in a one-

step experiment. In this method, NPs are simultaneously produced and dispersed into the base fluid medium, which can prominently decrease the agglomeration and enhance the stability of NP–stabilized MEs.[33,34]

Nanoparticles have several applications in the environmental and petroleum industries. For example, subsurface flooding with NPs and nanofluids is able to increase production from oil reservoirs due to the high interfacial activity of NPs. The large surface area to volume ratios of NPs enable them to adsorb at fluid-fluid interfaces and lower IFT.[35–37] The IFT reduction is further promoted in the presence of surfactants by the creation of stable interfacial complexes,[29] resulting in the formation of smaller oil droplets.[38] The enhanced emulsification ability depends on the properties and amounts of NPs. With increasing NP to oil mass ratio, the size of emulsified oil droplets decreases.[39] Nanoparticles have also the ability to alter the wettability of solid surfaces through their self-structuring behavior.[40–43] The latter increases the structural disjoining pressure in the confined three-phase contact region, especially near the tip of the wedge. With the increasing structural disjoining pressure, NPs can move the NAPL/water interface forward, alter the wettability, and consequently detach NAPL from surfaces.[43] This behavior was observed in several outcrop and reservoir rocks. In sandstones, SiO_2 and TiO_2 NPs were reported to enhance oil recovery due to both wettability alteration and IFT reduction.[35,44,45] The deposition of NPs could plug the water channels and increase the sweep efficiency during the floodings.[46,47] Similarly, SiO_2, Al_2O_3, and TiO_2 NPs were reported to improve oil recovery from carbonates due to viscosity modification, IFT reduction, and wettability alteration.[18,35,36,48] Using nanofluids could further enhance the performance of brine injection. Soil core data indicated that approximately 70% of the prevalent NAPL was removed after NP-stabilized emulsion flooding.[49] Recently, Hu and co-workers proposed a novel method to synthesize NPs *in-situ* in MEs. The new formulation significantly increased the oil displacement efficiency with an additional NAPL recovery of about 19% compared to ME alone. The NP-stabilized ME exhibited stable adsorption at the oil/water interface, synergistic stabilization effects between NP and surfactant, and increased brine phase viscosity.[29]

While NP-stabilized MEs often outperformed MEs alone, there are only limited studies available on their displacement mechanism in porous media and the types of fluid-fluid and fluid-rock interactions involved. For example, the impact of rock properties (pore geometry, topology, mineralogy, and surface texture) on these interfacial interactions is still not clear, especially at microscale. The goal of this study was to understand the impact of ME stabilized by *in-situ* synthesized NP (MENP) on the pore-scale displacement physics of NAPL in a heterogeneous aquifer sandstone (Arkose). A novel method was developed to synthesize SiO_2 *in-situ* in a ME and investigate its impact on the displacement efficiency of NAPL in Arkose using x-ray microtomography combined with a core flooding system. Novel insights are gained on the superior ability of MENP to alter the wettability of rough carbonate cements and mobilize NAPL through pores with small radius or complex geometry.

2. EXPERIMENTAL MATERIALS AND METHODS

2.1 Materials

2.1.1 Rock

The rock used in this study was an outcrop from Arkose formation in east Colorado and Wyoming. One mother core 38 mm in diameter was drilled from the Arkose block, and then dried at 110 ^{o}C for 24 hours. After cooling down to ambient temperature, the porosity and permeability of the core were measured using a Helium porosimeter-permeameter apparatus (AP -608, Coretest system), which were 17% and 26 mD, respectively. Two miniature core samples, both 5 mm in diameter and 47 mm in length, were drilled from the mother core to be used in the core-flooding experiments. The absolute brine permeabilities of the miniature cores were measured to be 26 mD and 32 mD, respectively. The porosities were measured using the histogram thresholding method and found to be 17% and 16.84%.

2.1.2 Fluids

We used a medium crude oil from Gibbs field (Minnelusa formation) of Wyoming with 10.2% asphaltene as the NAPL in this study. The oil was centrifuged at 6,000 rpm for one hour and then filtered through a 0.5 μm filter to remove possible debris. The brine was composed of 1 M $CaCl_2$ in distilled-deionized water, which was selected in a previous study.[50] NaI dopant (>99%, Sigma Aldrich) was added to the brine at a concentration of 7 wt% to enhance its contrast with NAPL phase in the micro-CT images.

2.2 Methods

2.1.3 Microemulsions stabilized by surfactants (ME) and *in-situ* synthesized NPs (MENP)

To stabilize MEs of d-limonene (96.9%, MP Biomedicals) in brine, we used Triton X-100 (laboratory grade, Sigma Aldrich) and n-dodecyl β- D-maltoside (>98%, Sigma Aldrich) as emulsifying agents and 2-propanol (ACS grade, Fisher Scientific) as co-surfactant. The Triton/maltoside/d-limonene/2-propanol blend was mixed with a weight ratio of 2:2:1:0.8. Afterward, brine was added to the mixture in two steps: 1) until the water content is 15 wt%, stirred at 200 rpm for 10 min, 2) until brine content is 99.5%, stirred at 500 rpm for 10 min. The ME was transparent with a total surfactant concentration of 0.33 wt%. The detailed preparation procedures are provided in previous studies.[8,9,51]

In order to synthesize the SiO_2 NP *in-situ* at the d-limonene/water interfaces in ME, we selected tetraethyl orthosilicate (>99%, Sigma Aldrich) as the oil-soluble precursor. It was first dissolved in d-limonene and then the mixture was used as the hydrocarbon phase to prepare surfactant-stabilized ME following the procedure described previously. The surfactant-stabilized oil droplets could act as nano-reactors to control the sol-gel reaction between water and tetraethyl orthosilicate as shown in Equation 1.[52] After contacting with water, tetraethyl orthosilicate formed silanol groups by hydrolysis and subsequently developed siloxane bridges by a condensation reaction, which resulted in the formation of single monodisperse nano-sized SiO_2 particles.[52–55]

$$Si(OC_2H_5)_4 + 2H_2O \rightarrow SiO_2 \downarrow + 4C_2H_6O \qquad (1)$$
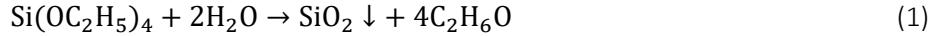
The amount of tetraethyl orthosilicate was pre-determined so that the final concentration of NPs in ME could reach 0.01 wt%. NaOH solution (> 97.0%, Fisher Scientific) was added slowly into the ME as a catalyst via a syringe pump and mixed by an ultrasound probe with an amplitude of 25 until the pH of the solution reached 10. After reacting at 60 °C for seven days, the solution was titrated by diluted hydrochloric acid (36.5-38.0%, Fisher Scientific) until pH decreased back to 7. Finally, $CaCl_2$ was added until its concentration reached 1 M.

2.1.4   Morphology and stability analysis

In order to visualize the morphology of the ME and MENP, an Environmental Transmission Electron Microscope (Titan ETEM G2, FEI) was used at 220 kV. ME and MENP were carefully transferred on silicon dioxide coated carbon TEM grids (Ted Pella) and dried overnight at ambient conditions before the TEM imaging process. ImageJ software was used to analyze the micrographs. The average droplet sizes were measured based on the diameters of over 30 different droplets. The thermal stability of ME and MENP was also investigated using a sedimentation method. ME and MENP were placed in closed bottles at 25°C, 60°C, and 80 °C for seven days before examining their phase separation behavior.

2.1.5   Dynamic interfacial tension and droplet size distribution

The dynamic IFT between NAPL and different brine solutions (1 M $CaCl_2$, ME, MENP) was measured by pendant drop tensiometry according to a procedure described elsewhere.[8] The needle diameter was selected between 0.711 and 1.762 mm to ensure a Bond number close to unity. The images were captured every 1 min and analyzed by the Axisymmetric Drop Shape Analysis (ADSA) software. In order to evaluate the emulsification ability of ME and MENP, NAPL and brine solutions (50/50 vol ratio) were mixed for 5 h at a speed of 500 rpm. The rag layers between the NAPL and brine phases were diluted 20 times by the

same brine solutions to enhance their transparency to light. The droplet size of the resulting emulsions was visualized by an inverted microscope (IX83, Olympus) and analyzed by ImageJ software. More than two hundred different droplets were evaluated for the droplet size analysis of each solution.

2.1.6 Mineralogy and pore size distribution

The mineralogy of Arkose sandstone was evaluated using Quantitative Evaluation of Minerals by Scanning Electron Microscopy (QEMSCAN 650F, FEI). The SEM images were captured at 25 kV and 6.2 nA. A Species Identification Protocol was used to convert the raw data to a 3.0 × 3.0 mm mineralogy map with a resolution of 0.73 μm per pixel. The fraction of different minerals were further analyzed quantitatively and then used to identify the major minerals in micro-CT images of the miniature core samples. The pore size distribution of the Arkose rock was evaluated using a micro-CT scanner (VERSA-XRM500, Zeiss) with a resolution of 1.9 μm per pixel. The x-ray source was operated at a voltage of 90 kV and a power of 6 W. After acquiring the micro-tomographic images of the sample, the raw data were then segmented and analyzed using Avizo Fire 9.4 software.

2.1.7 Miniature core flooding experiments

Microscale core flooding experiments were conducted with a miniature core flooding system integrated with a high-resolution X-ray micro-CT scanner (VERSA-XRM500, Zeiss). Figure S1(a) of the Supporting Information shows a schematic diagram of the experimental setup. One pulse-free Quizix pump was used to maintain the overburden pressure inside the high-pressure miniature core holder. Other two Quizix pumps were used to inject NAPL and brine phases separately from the bottom of the core. The produced liquids were received from the top of the core at the constant back pressure. The center of the cores, a cylindrical field of view with 4 mm in diameter and 4 mm in length, was scanned at a resolution of

2.12 microns during the flooding tests. X-ray source exposure time and voltage were selected to reduce the noise and enhance the quality of the micro-tomographic images.

To examine the pore-scale displacement mechanisms during ME and MENP flooding, two miniature Arkose cores were used and flooded by ME and MENP, separately. Figure S1(b) of the Supporting Information shows a schematic of the experimental procedure applied for each flooding test. For each set of experiment, the Arkose core was first placed in a miniature core holder with a confining pressure of 200 psi. Afterward, a location of interest in the middle of the core was scanned at a resolution of 2.12 μm per voxel to generate reference images. After injecting CO_2 into the flooding system for one hour, the tubings and the core were vacuumed for 24 hours and then saturated with brine. Several pore volumes of brine were subsequently injected at 200 psi to dissolve all the trapped CO_2 in the brine phase. Next, NAPL was injected at a flow rate of 0.001 cc/min to establish the initial brine saturation. After aging the core dynamically with an oil flow rate of 0.0002cc/min at 60 °C for seven days, water flooding was conducted followed by ME or MENP flooding at the same back pressure and a flow rate of 0.01 cc/min. The back pressure and confining pressure were maintained at 200 psi and 400 psi, respectively, for each flooding tests. The same location of interest was scanned at the end of each flooding, i.e., primary drainage, water flooding, ME flooding, and MENP flooding.

2.1.8　Data acquisition and image analysis

In order to examine the microscale displacement mechanisms that control fluid flow through porous media, the tomography images acquired by the micro-CT scanner were then reconstructed to generate pore maps and fluid occupancy maps using Avizo Fire 9.4 software.[56] During data processing, the raw data were first smoothened to reduce the noises using the non-local means filter. [57] The reference images of the dry core sample were then segmented into pore maps, which presented the pore topology of the Arkose rock. Each wet image set acquired after primary drainage, water flooding, and chemical flooding

was manually registered to the reference image set pixel-by-pixel. After eliminating the grains from the wet images, the wet image sets were segmented into the brine and NAPL phases to obtain fluid occupancy maps by applying the histogram threshold method. The fluid occupancy maps were then used directly to measure the *in-situ* contact angles. For each mineral, *in-situ* contact angles were evaluated with over forty NAPL droplets in different locations of the core. The selected droplets were examined in ten consecutive slides to identify the NAPL/brine/mineral contact line. The slice-averaged saturations of brine and size distributions of NAPL clusters were analyzed using statistical analysis methods.

3. RESULTS

3.1 Rock characterization

Arkose sandstone is a heterogeneous rock with respect to mineralogy and pore topology. It consists of 58.7% quartz, 27.6% carbonate (calcite and dolomite), 7.72% feldspar and a small fraction of other minerals such as albite, illite, pyrite, etc., as shown in Figure 1 and listed in Table S1 of the Supporting Information. The thin section analysis of this rock indicates that dolomite is mainly present in the form of microporous cement. Figure 1 also displays the micro-CT image of Arkose from which pore topology is determined. The pore size distribution has two peaks at about 45 µm and 95 µm. This indicates that the rock has narrow throats and relatively larger pores, which makes it easier to trap NAPL. To understand whether the scanned field of view (FOV) is within porosity based representative elementary volume (REV), the porosities of cubical sub-volumes with various lengths from 0.1 to 2.3 mm were calculated in Figure S2. The porosity varied significantly until the cubical sub-volume lengths were large than 1.2 mm. Therefore, the porosity estimated within the FOV can represent the overall values of the core sample.

3.2 Microemulsion phase behavior

The pseudo-ternary phase diagram in Figure S3 of the Supporting Information illustrates the preparation history and phase behaviors of MEs. Surfactant triton, maltoside and alcohol were mixed at a fixed weight ratio of 2/2/0.8 to form S_{mix}. D-limonene was then added at different weight ratios (1/9 to 9/1) and the phase diagram was obtained by titrating these mixtures with brine at different concentrations (10% to 90%). In the figure, the dashed arrow indicates the path of microemulsion dilution in brine until the 0.33 wt% surfactant concentrations were reached. We found that triton, maltoside, d-limonene, brine, and 2-propanol blended at a specific weight ratio of 2/2/1/1/0.8 provided stable and transparent MEs over a period of 6 months at ambient conditions. When S_{mix} to d-limonene ratio was lower than 3/7 (area below the red dashed line), milky white oil-in-water (o/w) emulsions formed with increasing water content. In contrast, when S_{mix} to d-limonene ratio was higher than 3/7 (area above the red dashed line), transparent MEs were obtained. The high concentration of S_{mix} contributed to stronger emulsification capability, which promoted the formation of MEs.

3.3 TEM micrographs and thermal stability

TEM micrographs of the nanofluids are provided in Figure 2 where the morphology of microemulsions and nanoparticles can be visualized. The average sizes of d-limonene droplets in ME and MENP were 85 nm and 71 nm, respectively. Beside surfactant molecules, a large number of small NPs (seen as dark dots) adsorbed at d-limonene/water interfaces with an average diameter of 3.2 nm. This is because d-limonene droplets acted as nano-reactors for the sol-gel reaction between water and oil-soluble tetraethyl orthosilicate.[58,59] The two precursors reacted at the interface upon contact to form SiO_2 NP. After their *in-situ* synthesis, the NPs preferred to stay at the oil/water interface and formed a steric barrier to droplet coalescence.[29] The stability of nanofluids at various temperatures was also examined using the sedimentation method described in the Methods section (Figure 3). Both ME and MENP remained

transparent and stable at 25 °C and 60 °C for seven days. However, ME started to form larger oil droplets at 80 °C due to the coalescence of natural oil droplets and consequently became cloudy. MENP, in contrast, was still stable and transparent thanks to the steric barrier provided by NPs.

3.4 Dynamic interfacial tension and drop size distribution

The effect of nanofluids on the dynamic IFT between NAPL and brine was examined at 200 psi and 60 °C. Without any chemical additive, the IFT was about 21.1 mN/m after 200 min. It sharply decreased to 0.79 mN/m after the addition of ME (Figure 4). The amphiphilic structure of surfactants in ME made it energetically favorable to form a surfactant layer at the NAPL/water interface. D-limonene molecules acted as solvent for NAPL,[17,60] whereas 2-propanol was able to partition between NAPL and brine phases, change the polarity, and consequently decrease IFT.[61] The IFT between brine and NAPL was further reduced to 0.6 mN/m in the presence of nanoparticles. The mixture exhibited a faster diffusion rate to the interface, resulting in sharper IFT reduction with lower equilibrium values.[62]

Figure 5 shows the size distribution of NAPL droplets measured by optical microscopy with a maximum error of 10%. The droplets were extracted from the diluted rug layers according to the procedures described in Section 2.2.3. In ME, NAPL droplets had a bimodal distribution with two peaks at about 20 μm and 135 μm, respectively. The addition of MENP could significantly reduce the size of NAPL droplets (D=19 μm) and make them less polydisperse, in agreement with previous work.[38] The smaller droplet sizes provided larger interfacial surface areas where NPs and surfactants interacted to form rigid layers that constitute a mechanical barriers against coalescence.[20–23]

3.5 *In-situ* contact angle

During the dynamic aging process, surface-active NAPL molecules adsorbed on the pore walls, altering their wettability from water-wet to neutral or NAPL-wet.[50,63] Since wettability depends on rock mineralogy,

it will vary at the pore-scale in heterogeneous rocks. Figure 6 reveals that the wettability of quartz was altered to weakly NAPL-wet with an average *in-situ* CA of 112°. The contact angle distribution of NAPL droplets spanned over a relatively wide range of values (i.e., from 75° to 155°). This indicated that a small fraction of the pore surfaces was neutral-wet while a larger fraction became NAPL-wet. In contrast, all carbonate mineral surfaces were altered to NAPL-wet with an average *in-situ* CA of 139°. This could be explained by the formation of strong chemical bonds between carbonate surfaces and carboxylate groups of NAPL molecules, which contributed to a larger amount of NAPL adsorption.

Figure 6(b) reveals that the addition of ME into the brine phase could reverse the wettability of quartz and carbonate surfaces from NAPL-wet back to water-wet state with an average contact angle of 55° and 70°, respectively. The presence of nanoparticles in ME further reduced these angles to 51° and 56° and provided narrower distributions especially in carbonates (Figure 6(c)). A close examination of the micro-CT images in Figure 7 indicates that MENP could solubilize more NAPL from dolomite cement than ME. These rough surfaces are usually difficult to access due to their microporous nature.

3.6 Primary drainage

The water saturation profiles in the FOV at the end of each flooding cycle are shown in Figure 8. The NAPL (i.e., crude oil) was injected into the 100% water-saturated core samples until the average initial water saturation of 22.1% and 22.5% was established in two Arkose core samples. The average saturation was calculated from about 2,000 slides in the FOV. The initial water saturation was comparable across the first core, which indicated that the pore topology and mineralogy were consistent in different spots in the first core sample. The slight fluctuation of S_w in the second core may be due to variations in rock properties across the porous medium. The mineral surfaces of Arkose sandstone were initially water-wet. Therefore, the pore-scale piston-like displacements started from the larger pores with smaller threshold capillary pressures and then gradually moved into smaller capillary elements. Figure 9 shows two- and three-

dimensional images of the pore spaces at the end of primary drainage. The NAPL phase (in red) occupied the center of large pores. In contrast, most of the brine phase remained in small pores or corners of the pores.

3.7   Water flooding

After dynamic aging with NAPL at 0.0002 cc/min and 60 °C for seven days, the cores were flooded with brine as a secondary recovery method. During this process, brine displaced NAPL by piston-like and pore-body filling mechanism, and snap-off was less favorable at pore-scale due to the non-water wetting preference of the medium.[64] Figure 8 indicates that the water saturation reached 42% after water flooding. The large fraction of NAPL left in the rock is due to the low capillary number of the flow process and negative threshold capillary pressure in the rock. Note that a brine flow rate of 0.01 cc/min (capillary number = 3.5 x 10^{-7}) was applied to ensure that the flow was under capillary-dominated flow regime. Since the viscous pressure gradient was negligible, the sequence of pore-scale displacement was dominated by the threshold capillary pressure of each element, which is a function of wettability and pore radius. After aging, quartz and carbonate grains were mostly NAPL-wet. Therefore, the brine pressure needed to first overcome the negative threshold capillary pressure of each pore then fill the elements through piston-like displacement. The drainage process started from the larger pores with smaller threshold capillary pressures and then occurred in smaller ones. This displacement order was confirmed in Figure 9. The micro-CT images in this figure indicate that water could only occupy the center of large pores and bypassed small ones that required a greater pressure to invade. To further examine the amount of NAPL removal from various pore sizes, the volume fraction of residual NAPL was quantified in Figure 10 as a function of pore radius. Medium-sized pores with radii about 100 μm had the highest contribution to NAPL removal after water flooding. This is because the medium-sized pores constituted the largest fraction of the total pore volume (Figure 1),

and therefore contained most of the NAPL. They were also easier to invade than smaller pores due to their favorable threshold capillary pressure.

3.8 ME flooding

After the remaining NAPL saturation reached equilibrium at 45.1% in the first Arkose core, ME was injected at the same flow rate of 0.01 cc/min until the flow reached steady state condition. Figure 8 shows that the water saturation was further increased to 65.1% upon introduction of ME. In other words, ME flooding removed an additional 20% of NAPL after water flooding. This increase in NAPL recovery was driven by IFT reduction, wettability alteration, and emulsification capability of ME, in agreement with previous work.[9] The sharp decline of IFT from 21.1 to 0.79 mN/m (Figure 4) promoted the formation of very small NAPL droplets (Figure 5) that could easily flow through the rock. The addition of ME into the brine also reversed the wettability towards water-wet state (Figure 6) resulting in positive threshold capillary pressures, which made it energetically favorable to mobilize NAPL. Figure 9 confirms that ME flooding could efficiently mobilize and solubilize more NAPL, especially in sharp corners of NAPL-wet pores. However, most of these effects occurred in medium (50-130 µm) and large (130-200 µm) pores where the average contact angle decreased by up to 75° (Figure 10(a,c)).

3.9 MENP flooding

MENP was injected into the second Arkose core at 0.01 cc/min after water flooding to examine the impact of nanoparticles on fluid displacement. Figure 8 shows that an additional 34.3% of NAPL was produced by using MENP compared to brine alone, which was also 14.3% higher than the amount of NAPL removed by ME. The addition of MENP into the brine contributed to a faster reduction in the threshold capillary pressure upon contact with NAPL (Figures 4,5), resulting in a higher amount of NAPL mobilization.[65] The superior ability of MENP to restore the wettability of surfaces (especially in carbonates)

also led to a higher solubilization propensity (Figures 6,7). Figure 9 reveals that MENP was able to remove NAPL from small capillary elements (small pores, corners of large pores, micropores in cement, and pores with complex geometry). This observation was quantitatively confirmed in Figure 10(b) where the fraction of NAPL removal by MENP occurred in smaller pores, compared to water and ME floodings. The unique ability of MENP to penetrate these pores was also reflected in Figure 10(d) where CA was constant (about 53°) regardless of pore size. This behavior may have affected the sequence of displacement within the medium. Instead of invading large/medium pores only, MENP helped deliver surfactant molecules into both large/medium and small pores, modifying the displacement order and contributing to a stronger wettability alteration in micropores with large surface area such as carbonate cements.[66]

3.10 Residual NAPL cluster analysis

The effect of ME and MENP flooding on NAPL cluster sizes was further investigated by plotting the cluster size distribution curves of the residual NAPL at the end of each flooding (Figure 11). Although ME could effectively emulsify NAPLs and reduce their average sizes, there was still a portion of droplets with radii higher than 50 μm that could not penetrate small pores and narrow throats. This portion was significantly reduced with MENP and corroborates our previous findings (Figures 8-10). The presence of nanoparticles enhanced the steric stabilization of NAPL clusters leading to the formation of smaller ones. To further investigate the cluster size distribution of NAPL, the cumulative size distribution M(s) was plotted against cluster volume as shown in Figure 12. There is a power-law relationship between number of clusters N(s) and cluster size (s) in a capillary-dominated flow regime (Equation 2).[67,68]

$$\text{M(s)} = \sum_s^\infty sN(s) \sim s^{-\tau+2}$$

(2)

The distribution exponent τ can be calculated based on the slope of a linear fit to log (s) versus log M(s) plots.[67] Very small and large clusters are truncated from the data set. The τ for the water flooding (2.13)

was close to that predicted by the percolation theory (2.19). [69] After introduction of ME and MENP, the τ value was increased to 2.33 and 2.55, respectively. This indicates that both ME and MENP could form smaller oil globules in the porous medium due to the promoted mobilization and solubilization capability of these additives. This behavior was further confirmed in Figure 13 where the surface area of each cluster was plotted against its volume. The power-law correlation between the surface area and volume was examined to provide more insight onto the impact of MENP on NAPL cluster size. The calculated p for water flooding is 0.78, which is consistent with previous studies[67] and smaller than the value predicted by the percolation theory.[70] However, after ME and MENP flooding, the p became higher with values of 0.81 and 0.84, respectively. This indicated that the corresponding surface area became larger at a given cluster volume after introduction of ME and MENP, which could benefit the mass transfer between NAPL and chemical solutions, enhance NAPL displacement and consequently reduce the residual NAPL saturation.[71]

4. CONCLUSIONS

The impact of microemulsions stabilized by surfactants and *in-situ* synthesized nanoparticles on NAPL displacement in a heterogeneous aquifer rock was examined using microtomography integrated with miniature core flooding, and compared to results with brine and microemulsions stabilized by surfactants alone. A systematic analysis of the IFT values, drop size distribution, *in-situ* contact angle distribution, saturation profiles, fluid occupancy, and cluster size distribution after each flooding was used to explain the NAPL displacement mechanisms observed inside the rock. Compared to ME alone, nanoparticles in MENP could synergistically interact with surfactant molecules to adsorb at oil/brine interfaces and form stable pickering emulsions. The rapid drop in IFT contributed to a faster reduction in the threshold capillary pressure upon contact with NAPL, resulting in the formation of smaller droplets that were easily mobilized. The latter were also able to penetrate small capillary elements of the rock (such as pore corners, pores with complex geometries, and microporous carbonate cements) that were not fully accessible to ME and restore

their wettability, thereby promoting even more NAPL solubilization. Thus, the enhanced mobilization and solubilization ability of MENP were the key parameters controlling the improved NAPL displacement in the aquifer rock. Together, they almost doubled the amount of NAPL cleanup, compared to waterflooding. The new formulated nanoparticle-surfactant systems are also considered suitable for enhancing oil recovery; particularly in heterogeneous reservoirs containing microporous carbonate cements.

5. ACKNOWLEDGMENTS

6. REFERENCES

(1)   Bennion, D. B.; Thomas, F. B.; Bietz, R. F.; Bennion, D. W. Water And Hydrocarbon Phase Trapping In Porous Media-Diagnosis, Prevention And Treatment. *J. Can. Pet. Technol.* **1996**, *35* (10). https://doi.org/10.2118/96-10-02.

(2)   Buckley, J. S.; Liu, Y.; Monsterleet, S. Mechanisms of Wetting Alteration by Crude Oils. *SPE J.* **1998**, *3* (01), 54–61. https://doi.org/10.2118/37230-PA.

(3)   Kumar, M.; Fogden, A.; Senden, T.; Knackstedt, M. A. Investigations of Pore-Scale Mixed Wettability; Society of Petroleum Engineers, 2010. https://doi.org/10.2118/129974-MS.

(4)   Rosen, M. J.; Wang, H.; Shen, P.; Zhu, Y. Ultralow Interfacial Tension for Enhanced Oil Recovery at Very Low Surfactant Concentrations. *Langmuir* **2005**, *21* (9), 3749–3756. https://doi.org/10.1021/la0400959.

(5)   Sharma, M. K.; Shah, D. O.; Brigham, W. E. The Influence of Temperature on Surface and Microscopic Properties of Surfactant Solutions in Relation to Fluid Displacement Efficiency in Porous Media. *AIChE J.* **1985**, *31* (2), 222–228. https://doi.org/10.1002/aic.690310208.

(6)   Standnes, D. C.; Austad, T. Wettability Alteration in Chalk: 2. Mechanism for Wettability Alteration from Oil-Wet to Water-Wet Using Surfactants. *J. Pet. Sci. Eng.* **2000**, *28* (3), 123–143. https://doi.org/10.1016/S0920-4105(00)00084-X.

(7)   Standnes, D. C.; Austad, T. Wettability Alteration in Carbonates: Interaction between Cationic Surfactant and Carboxylates as a Key Factor in Wettability Alteration from Oil-Wet to Water-Wet Conditions. *Colloids Surf. Physicochem. Eng. Asp.* **2003**, *216* (1), 243–259. https://doi.org/10.1016/S0927-7757(02)00580-0.

(8)   Qin, T.; Javanbakht, G.; Goual, L.; Piri, M.; Towler, B. Microemulsion-Enhanced Displacement of Oil in Porous Media Containing Carbonate Cements. *Colloids Surf. Physicochem. Eng. Asp.* **2017**, *530*, 60–71. https://doi.org/10.1016/j.colsurfa.2017.07.017.

(9)   Javanbakht, G.; Arshadi, M.; Qin, T.; Goual, L. Micro-Scale Displacement of NAPL by Surfactant and Microemulsion in Heterogeneous Porous Media. *Adv. Water Resour.* **2017**, *105*, 173–187. https://doi.org/10.1016/j.advwatres.2017.05.006.

(10)   McClements, D. J. Nanoemulsions versus Microemulsions: Terminology, Differences, and Similarities. *Soft Matter* **2012**, *8* (6), 1719–1729. https://doi.org/10.1039/C2SM06903B.

(11)   Ezrahi, S.; Aserin, A.; Garti, N. Aggregation Behavior in One-Phase (Winsor IV) Microemulsion Systems. *Handb. Microemulsion Sci. Technol. N. Y. Inf. Inc* **1999**, 185–246.

(12)   Karambeigi, M. S.; Nasiri, M.; Haghighi Asl, A.; Emadi, M. A. Enhanced Oil Recovery in High Temperature Carbonates Using Microemulsions Formulated with a New Hydrophobic Component. *J. Ind. Eng. Chem.* **2016**, *39*, 136–148. https://doi.org/10.1016/j.jiec.2016.05.020.

(13)   Bera, A.; Mandal, A. Microemulsions: A Novel Approach to Enhanced Oil Recovery: A Review. *J. Pet. Explor. Prod. Technol.* **2015**, *5* (3), 255–268. https://doi.org/10.1007/s13202-014-0139-5.

(14)   Jeirani, Z.; Jan, B. M.; Ali, B. S.; See, C. H.; Saphanuchart, W. Pre-Prepared Microemulsion Flooding in Enhanced Oil Recovery: A Review. *Pet. Sci. Technol.* **2014**, *32* (2), 180–193.

(15)   Castro Dantas, T. N.; Soares A, P. J.; Wanderley Neto, A. O.; Dantas Neto, A. A.; Barros Neto, E. L. Implementing New Microemulsion Systems in Wettability Inversion and Oil Recovery from Carbonate Reservoirs. *Energy Fuels* **2014**, *28* (11), 6749–6759.

(16)   Jeirani, Z.; Mohamed Jan, B.; Si Ali, B.; Noor, I. M.; See, C. H.; Saphanuchart, W. Formulation, Optimization and Application of Triglyceride Microemulsion in Enhanced Oil Recovery. *Ind. Crops Prod.* **2013**, *43*, 6–14. https://doi.org/10.1016/j.indcrop.2012.07.002.

(17)   Lowry, E.; Sedghi, M.; Goual, L. Molecular Simulations of NAPL Removal from Mineral Surfaces Using Microemulsions and Surfactants. *Colloids Surf. Physicochem. Eng. Asp.* **2016**, *506*, 485–494. https://doi.org/10.1016/j.colsurfa.2016.07.002.

(18)   Karimi, A.; Fakhroueian, Z.; Bahramian, A.; Pour Khiabani, N.; Darabad, J. B.; Azin, R.; Arya, S. Wettability Alteration in Carbonates Using Zirconium Oxide Nanofluids: EOR Implications. *Energy Fuels* **2012**, *26* (2), 1028–1036. https://doi.org/10.1021/ef201475u.

(19)   Yang, W.; Peters, J. I.; Williams, R. O. Inhaled Nanoparticles—A Current Review. *Int. J. Pharm.* **2008**, *356* (1), 239–247. https://doi.org/10.1016/j.ijpharm.2008.02.011.

(20)   Chevalier, Y.; Bolzinger, M.-A. Emulsions Stabilized with Solid Nanoparticles: Pickering Emulsions. *Colloids   Surf.   Physicochem.   Eng.   Asp.* **2013**, *439*, 23–34. https://doi.org/10.1016/j.colsurfa.2013.02.054.

(21)   Babak, V. G.; Stébé, M.-J. Highly Concentrated Emulsions: Physicochemical Principles of Formulation. *J. Dispers. Sci. Technol.* **2002**, *23* (1–3), 1–22. https://doi.org/10.1080/01932690208984184.

(22)   Vrij, A.; Overbeek, J. Th. G. Rupture of Thin Liquid Films Due to Spontaneous Fluctuations in Thickness. *J. Am. Chem. Soc.* **1968**, *90* (12), 3074–3078. https://doi.org/10.1021/ja01014a015.

(23)   Worthen, A. J.; Bryant, S. L.; Huh, C.; Johnston, K. P. Carbon Dioxide-in-Water Foams Stabilized with Nanoparticles and Surfactant Acting in Synergy. *AIChE J.* **2013**, *59* (9), 3490–3501. https://doi.org/10.1002/aic.14124.

(24)   Pei, H. H.; Zhang, G. C.; Ge, J. J.; Zhang, J.; Zhang, Q.; Fu, L. P. Investigation of Nanoparticle and Surfactant Stabilized Emulsion to Enhance Oil Recovery in Waterflooded Heavy Oil Reservoirs; Society of Petroleum Engineers, 2015. https://doi.org/10.2118/174488-MS.

(25)   Sun, Q.; Li, Z.; Li, S.; Jiang, L.; Wang, J.; Wang, P. Utilization of Surfactant-Stabilized Foam for Enhanced Oil Recovery by Adding Nanoparticles. *Energy Fuels* **2014**, *28* (4), 2384–2394. https://doi.org/10.1021/ef402453b.

(26)   Sharma, T.; Kumar, G. S.; Sangwai, J. S. Enhanced Oil Recovery Using Oil-in-Water (o/w) Emulsion Stabilized by Nanoparticle, Surfactant and Polymer in the Presence of NaCl. *Geosystem Eng.* **2014**, *17* (3), 195–205. https://doi.org/10.1080/12269328.2014.959622.

(27)   Sharma, T.; Kumar, G. S.; Sangwai, J. S. Comparative Effectiveness of Production Performance of Pickering Emulsion Stabilized by Nanoparticle–Surfactant–Polymerover Surfactant–Polymer (SP) Flooding for Enhanced Oil Recoveryfor Brownfield Reservoir. *J. Pet. Sci. Eng.* **2015**, *129*, 221–232. https://doi.org/10.1016/j.petrol.2015.03.015.

(28)   Zargartalebi, M.; Kharrat, R.; Barati, N. Enhancement of Surfactant Flooding Performance by the Use of Silica Nanoparticles. *Fuel* **2015**, *143*, 21–27. https://doi.org/10.1016/j.fuel.2014.11.040.

(29)   Hu, Z.; Nourafkan, E.; Gao, H.; Wen, D. Microemulsions Stabilized by In-Situ Synthesized Nanoparticles for Enhanced Oil Recovery. *Fuel* **2017**, *210*, 272–281. https://doi.org/10.1016/j.fuel.2017.08.004.

(30)   Nourafkan, E.; Gao, H.; Hu, Z.; Wen, D. Formulation Optimization of Reverse Microemulsions Using Design of Experiments for Nanoparticles Synthesis. *Chem. Eng. Res. Des.* **2017**, *125*, 367–384. https://doi.org/10.1016/j.cherd.2017.07.023.

(31)   Gupta, A.; Burak Eral, H.; Alan Hatton, T.; S. Doyle, P. Controlling and Predicting Droplet Size of Nanoemulsions: Scaling Relations with Experimental Validation. *Soft Matter* **2016**, *12* (5), 1452–1458. https://doi.org/10.1039/C5SM02051D.

(32)   Binks, B. P.; Rodrigues, J. A. Enhanced Stabilization of Emulsions Due to Surfactant-Induced Nanoparticle Flocculation. *Langmuir* **2007**, *23* (14), 7436–7439. https://doi.org/10.1021/la700597k.

(33)   Sanchez-Dominguez, M.; Pemartin, K.; Boutonnet, M. Preparation of Inorganic Nanoparticles in Oil-in-Water Microemulsions: A Soft and Versatile Approach. *Curr. Opin. Colloid Interface Sci.* **2012**, *17* (5), 297–305. https://doi.org/10.1016/j.cocis.2012.06.007.

(34)   Sanchez-Dominguez, M.; Koleilat, H.; Boutonnet, M.; Solans, C. Synthesis of Pt Nanoparticles in Oil-in-Water Microemulsions: Phase Behavior and Effect of Formulation Parameters on Nanoparticle Characteristics. *J. Dispers. Sci. Technol.* **2011**, *32* (12), 1765–1770. https://doi.org/10.1080/01932691.2011.616170.

(35)   Ehtesabi, H.; Ahadian, M. M.; Taghikhani, V.; Ghazanfari, M. H. Enhanced Heavy Oil Recovery in Sandstone Cores Using TiO$_2$ Nanofluids. *Energy Fuels* **2014**, *28* (1), 423–430. https://doi.org/10.1021/ef401338c.

(36)   Amraei, A.; Fakhroueian, Z.; Bahramian, A. Influence of New SiO2 Nanofluids on Surface Wettability and Interfacial Tension Behaviour between Oil-Water Interface in EOR Processes. *J. Nano Res.* **2014**, *26*, 1–8. https://doi.org/10.4028/www.scientific.net/JNanoR.26.1.

(37)   Ravera, F.; Santini, E.; Loglio, G.; Ferrari, M.; Liggieri, L. Effect of Nanoparticles on the Interfacial Properties of Liquid/Liquid and Liquid/Air Surface Layers. *J. Phys. Chem. B* **2006**, *110* (39), 19543–19551. https://doi.org/10.1021/jp0636468.

(38)   Eskandar, N. G.; Simovic, S.; A. Prestidge, C. Synergistic Effect of Silica Nanoparticles and Charged Surfactants in the Formation and Stability of Submicron Oil-in-Water Emulsions. *Phys. Chem. Chem. Phys.* **2007**, *9* (48), 6426–6434. https://doi.org/10.1039/B710256A.

(39) Melle, S.; Lask, M.; Fuller, G. G. Pickering Emulsions with Controllable Stability. *Langmuir* **2005**, *21* (6), 2158–2162. https://doi.org/10.1021/la047691n.

(40) Vafaei, S.; Borca-Tasciuc, T.; Podowski, M. Z.; Purkayastha, A.; Ramanath, G.; Ajayan, P. M. Effect of Nanoparticles on Sessile Droplet Contact Angle. *Nanotechnology* **2006**, *17* (10), 2523–2527. https://doi.org/10.1088/0957-4484/17/10/014.

(41) Ju, B.; Fan, T. Experimental Study and Mathematical Model of Nanoparticle Transport in Porous Media. *Powder Technol.* **2009**, *192* (2), 195–202. https://doi.org/10.1016/j.powtec.2008.12.017.

(42) Hendraningrat, L.; Li, S.; Torsæter, O. A Coreflood Investigation of Nanofluid Enhanced Oil Recovery. *J. Pet. Sci. Eng.* **2013**, *111*, 128–138. https://doi.org/10.1016/j.petrol.2013.07.003.

(43) Wasan, D. T.; Nikolov, A. D. Spreading of Nanofluids on Solids. *Nature* **2003**, *423* (6936), 156–159.

(44) Roustaei, A.; Saffarzadeh, S.; Mohammadi, M. An Evaluation of Modified Silica Nanoparticles' Efficiency in Enhancing Oil Recovery of Light and Intermediate Oil Reservoirs. *Egypt. J. Pet.* **2013**, *22* (3), 427–433. https://doi.org/10.1016/j.ejpe.2013.06.010.

(45) Kuang, W.; Saraji, S.; Piri, M. A Systematic Experimental Investigation on the Synergistic Effects of Aqueous Nanofluids on Interfacial Properties and Their Implications for Enhanced Oil Recovery. *Fuel* **2018**, *220*, 849–870. https://doi.org/10.1016/j.fuel.2018.01.102.

(46) Li, S.; Torsæter, O. An Experimental Investigation of EOR Mechanisms for Nanoparticles Fluid in Glass Micromodel. In *Paper SCA2014-022 was prepared for presentation at the International Symposium of the Society of Core Analysts held in Avignon, France*; 2014; pp 8–11.

(47) Hendraningrat, L.; Torsæter, O. Metal Oxide-Based Nanoparticles: Revealing Their Potential to Enhance Oil Recovery in Different Wettability Systems. *Appl. Nanosci.* **2015**, *5* (2), 181–199. https://doi.org/10.1007/s13204-014-0305-6.

(48) Giraldo, J.; Benjumea, P.; Lopera, S.; Cortés, F. B.; Ruiz, M. A. Wettability Alteration of Sandstone Cores by Alumina-Based Nanofluids. *Energy Fuels* **2013**, *27* (7), 3659–3665. https://doi.org/10.1021/ef4002956.

(49) Yang, G. C. C.; Chang, Y.-I. Integration of Emulsified Nanoiron Injection with the Electrokinetic Process for Remediation of Trichloroethylene in Saturated Soil. *Sep. Purif. Technol.* **2011**, *79* (2), 278–284. https://doi.org/10.1016/j.seppur.2011.03.004.

(50) Javanbakht, G.; Goual, L. Mobilization and Micellar Solubilization of NAPL Contaminants in Aquifer Rocks. *J. Contam. Hydrol.* **2016**, *185–186*, 61–73. https://doi.org/10.1016/j.jconhyd.2016.01.003.

(51) Goual, L.; Qin, T.; Javanbakht, G.; Piri, M. Microemulsions and Uses Thereof to Displace Oil in Heterogeneous Porous Media, June 2018.

(52)   Jiang, R.; Kunz, H. R.; Fenton, J. M. Composite Silica/Nafion® Membranes Prepared by Tetraethylorthosilicate Sol–Gel Reaction and Solution Casting for Direct Methanol Fuel Cells. *J. Membr. Sci.* **2006**, *272* (1), 116–124. https://doi.org/10.1016/j.memsci.2005.07.026.

(53)   Lindberg, R.; Sjöblom, J.; Sundholm, G. Preparation of Silica Particles Utilizing the Sol-Gel and the Emulsion-Gel Processes. *Colloids Surf. Physicochem. Eng. Asp.* **1995**, *99* (1), 79–88. https://doi.org/10.1016/0927-7757(95)03117-V.

(54)   Rao, K. S.; El-Hami, K.; Kodaki, T.; Matsushige, K.; Makino, K. A Novel Method for Synthesis of Silica Nanoparticles. *J. Colloid Interface Sci.* **2005**, *289* (1), 125–131. https://doi.org/10.1016/j.jcis.2005.02.019.

(55)   Stöber, W.; Fink, A.; Bohn, E. Controlled Growth of Monodisperse Silica Spheres in the Micron Size Range. *J. Colloid Interface Sci.* **1968**, *26* (1), 62–69. https://doi.org/10.1016/0021-9797(68)90272-5.

(56)   Mirchi, V. Pore-Scale Investigation of the Effect of Surfactant on Fluid Occupancies during Low-Salinity Waterflooding in Oil-Wet Carbonates; Society of Petroleum Engineers, 2018. https://doi.org/10.2118/194045-STU.

(57)   Li, Z.; Yu, L.; Trzasko, J. D.; Lake, D. S.; Blezek, D. J.; Fletcher, J. G.; McCollough, C. H.; Manduca, A. Adaptive Nonlocal Means Filtering Based on Local Noise Level for CT Denoising. *Med. Phys. 41* (1), 011908. https://doi.org/10.1118/1.4851635.

(58)   Okoli, C.; Sanchez-Dominguez, M.; Boutonnet, M.; Järås, S.; Civera, C.; Solans, C.; Kuttuva, G. R. Comparison and Functionalization Study of Microemulsion-Prepared Magnetic Iron Oxide Nanoparticles. *Langmuir* **2012**, *28* (22), 8479–8485. https://doi.org/10.1021/la300599q.

(59)   Nourafkan, E.; Asachi, M.; Gao, H.; Raza, G.; Wen, D. Synthesis of Stable Iron Oxide Nanoparticle Dispersions in High Ionic Media. *J. Ind. Eng. Chem.* **2017**, *50*, 57–71. https://doi.org/10.1016/j.jiec.2017.01.026.

(60)   Bui, K.; Akkutlu, I. Y.; Zelenev, A.; Saboowala, H.; Gillis, J. R.; Silas, J. A. Insights Into Mobilization of Shale Oil by Use of Microemulsion. *SPE J.* **2016**, *21* (02), 613–620. https://doi.org/10.2118/178630-PA.

(61)   Zana, R. Aqueous Surfactant-Alcohol Systems: A Review. *Adv. Colloid Interface Sci.* **1995**, *57*, 1–64. https://doi.org/10.1016/0001-8686(95)00235-I.

(62)   Fereidooni Moghadam, T.; Azizian, S. Effect of ZnO Nanoparticle and Hexadecyltrimethylammonium Bromide on the Dynamic and Equilibrium Oil–Water Interfacial Tension. *J. Phys. Chem. B* **2014**, *118* (6), 1527–1534. https://doi.org/10.1021/jp4106986.

(63) Qin, T.; Javanbakht, G.; Goual, L. Nanoscale Investigation of Surfactant-Enhanced Solubilization of Asphaltenes from Silicate-Rich Rocks. *Energy Fuels* **2018**. https://doi.org/10.1021/acs.energyfuels.8b03228.

(64) Landry, C. J.; Karpyn, Z. T.; Piri, M. Pore-Scale Analysis of Trapped Immiscible Fluid Structures and Fluid Interfacial Areas in Oil-Wet and Water-Wet Bead Packs. *Geofluids* **2011**, *11* (2), 209–227. https://doi.org/10.1111/j.1468-8123.2011.00333.x.

(65) Mirchi, V.; Saraji, S.; Akbarabadi, M.; Goual, L.; Piri, M. A Systematic Study on the Impact of Surfactant Chain Length on Dynamic Interfacial Properties in Porous Media: Implications for Enhanced Oil Recovery. *Ind. Eng. Chem. Res.* **2017**, *56* (46), 13677–13695. https://doi.org/10.1021/acs.iecr.7b02623.

(66) Nourafkan, E.; Hu, Z.; Wen, D. Nanoparticle-Enabled Delivery of Surfactants in Porous Media. *J. Colloid Interface Sci.* **2018**, *519*, 44–57. https://doi.org/10.1016/j.jcis.2018.02.032.

(67) Iglauer, S.; Wülling, W. The Scaling Exponent of Residual Nonwetting Phase Cluster Size Distributions in Porous Media. *Geophys. Res. Lett.* **2016**, *43* (21), 11,253-11,260. https://doi.org/10.1002/2016GL071298.

(68) Wilkinson, D. Percolation Effects in Immiscible Displacement. *Phys. Rev. A* **1986**, *34* (2), 1380–1391. https://doi.org/10.1103/PhysRevA.34.1380.

(69) Iglauer, S.; Favretto, S.; Spinelli, G.; Schena, G.; Blunt, M. J. X-Ray Tomography Measurements of Power-Law Cluster Size Distributions for the Nonwetting Phase in Sandstones. *Phys. Rev. E* **2010**, *82* (5), 056315. https://doi.org/10.1103/PhysRevE.82.056315.

(70) Iglauer, S.; Paluszny, A.; Blunt, M. J. Simultaneous Oil Recovery and Residual Gas Storage: A Pore-Level Analysis Using in Situ X-Ray Micro-Tomography. *Fuel* **2013**, *103*, 905–914. https://doi.org/10.1016/j.fuel.2012.06.094.

(71) Iglauer, S. Dissolution Trapping of Carbon Dioxide in Reservoir Formation Brine – A Carbon Storage Mechanism. *Mass Transf. - Adv. Asp.* **2011**. https://doi.org/10.5772/20206.
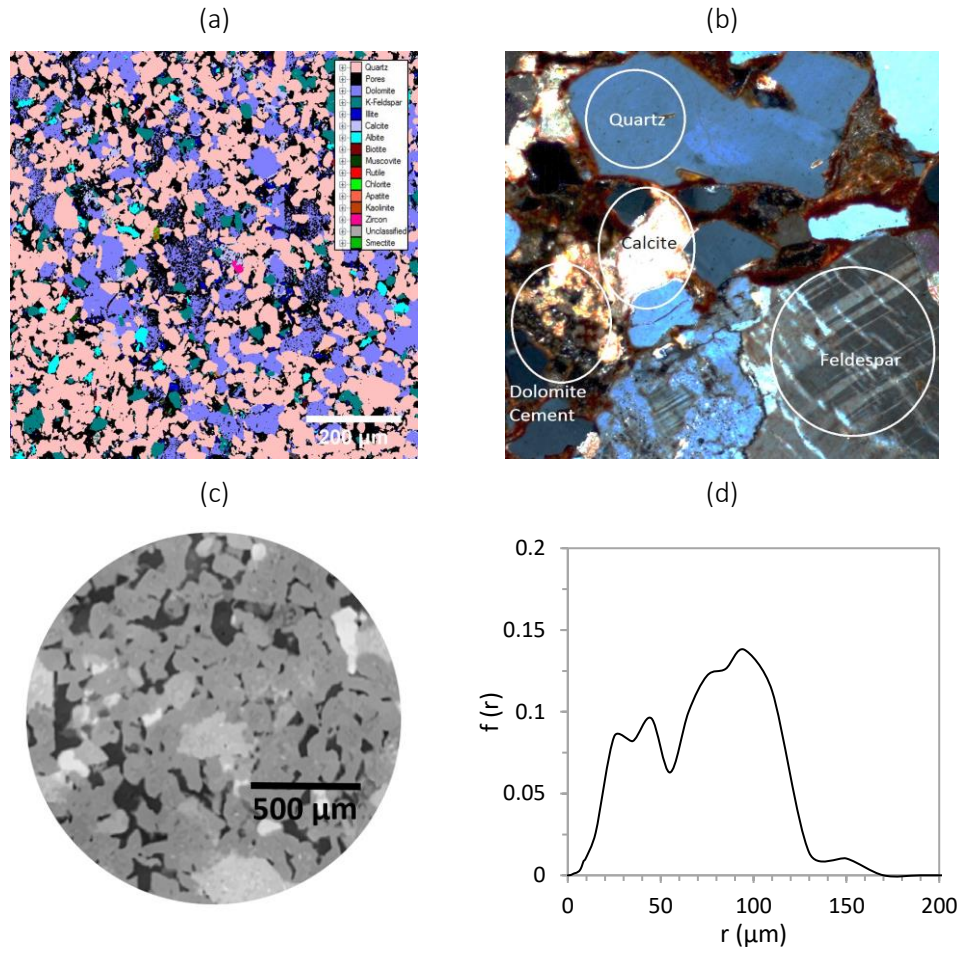
Figure 1. Characterization of Arkose rock: (a) Mineralogy map from QEMSCAN analysis, (b) Thin section analysis, (c) X-ray microtomographic image, and (d) Pore size distribution from (c).
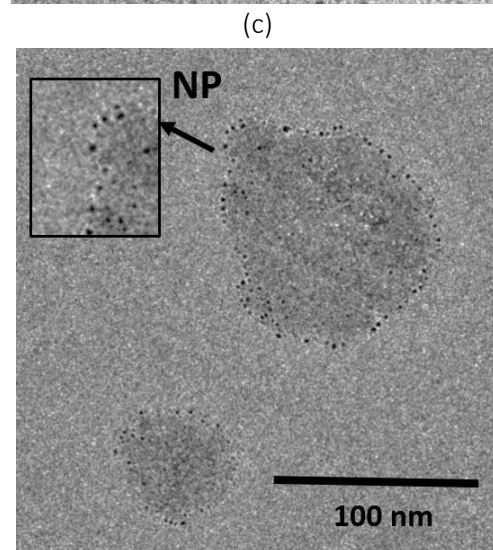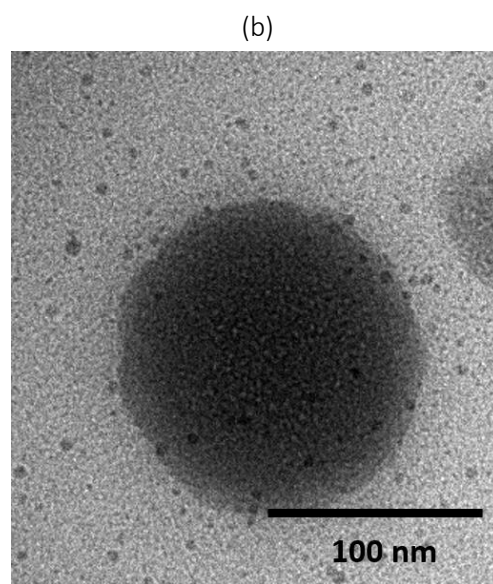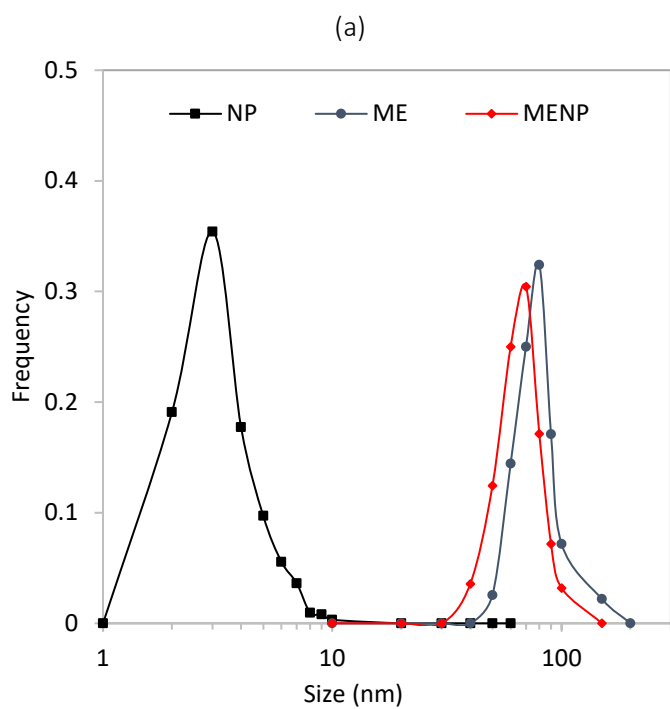
Figure 2. (a) Size distribution of NP, ME, and MENP, and TEM micrographs of (b) ME and (c) MENP with an average diameter of 85 nm and 71 nm, respectively. In MENP, NPs adsorbed at d-limonene/water interfaces have an average diameter of 3.2 nm.
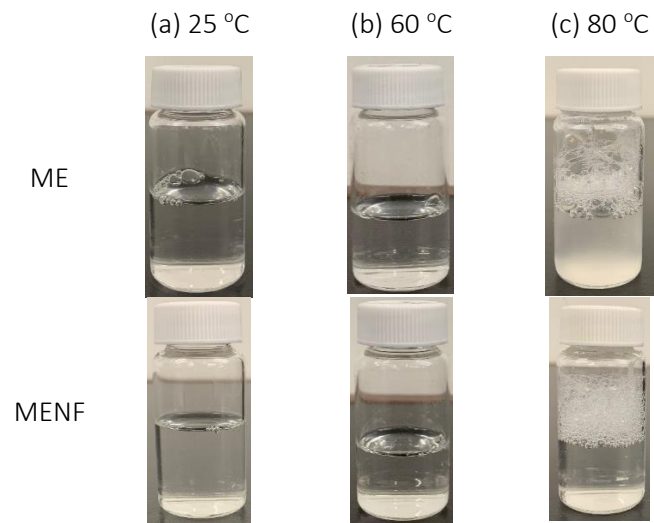
Figure 3. Sedimentation test results for ME (top) and MENP (bottom) at (a) 25 °C, (b) 60 °C, and (c) 80 °C after seven days. Transparent and colorless ME started to become cloudy after staying at 80 °C after seven days.
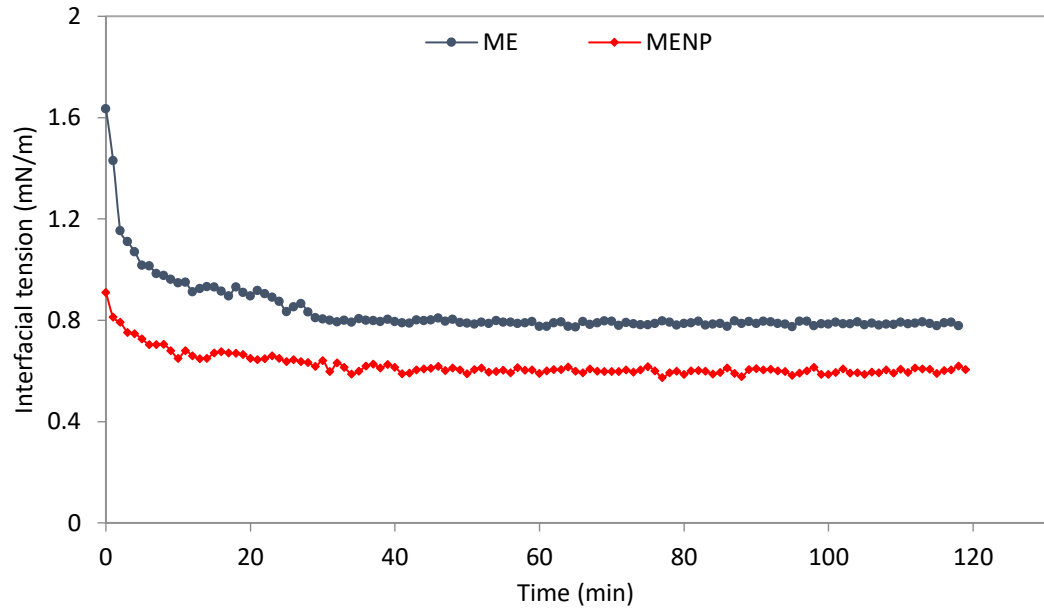
Figure 4. Dynamic interfacial tension between NAPL/ME and NAPL/MENP at 60° and 200 psi.
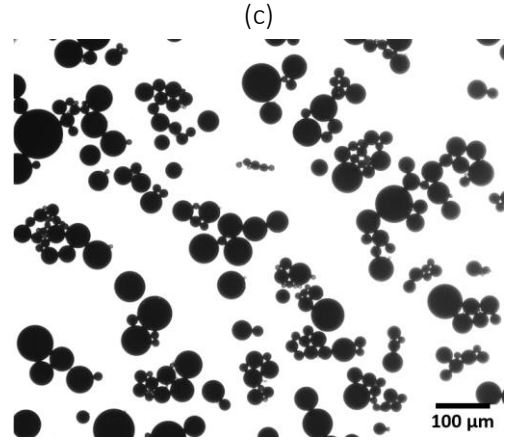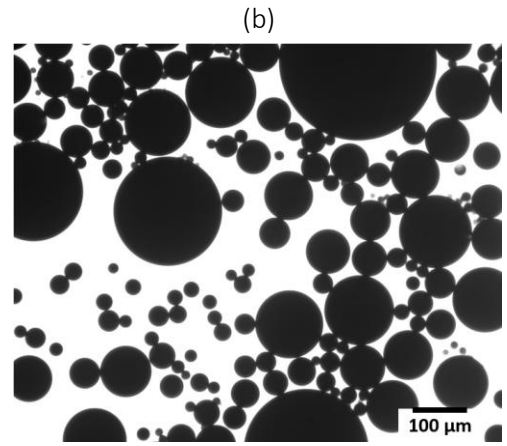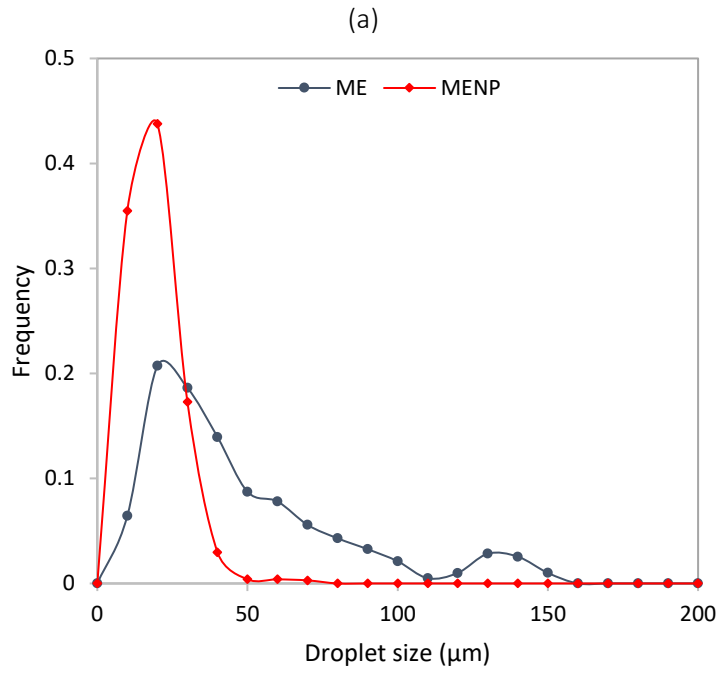
Figure 5. (a) Size distribution of NAPL droplets in diluted rag layer between NAPL and brine with ME and MENP. Microscopy images of these oil droplets in (b) ME and (c) MENP.
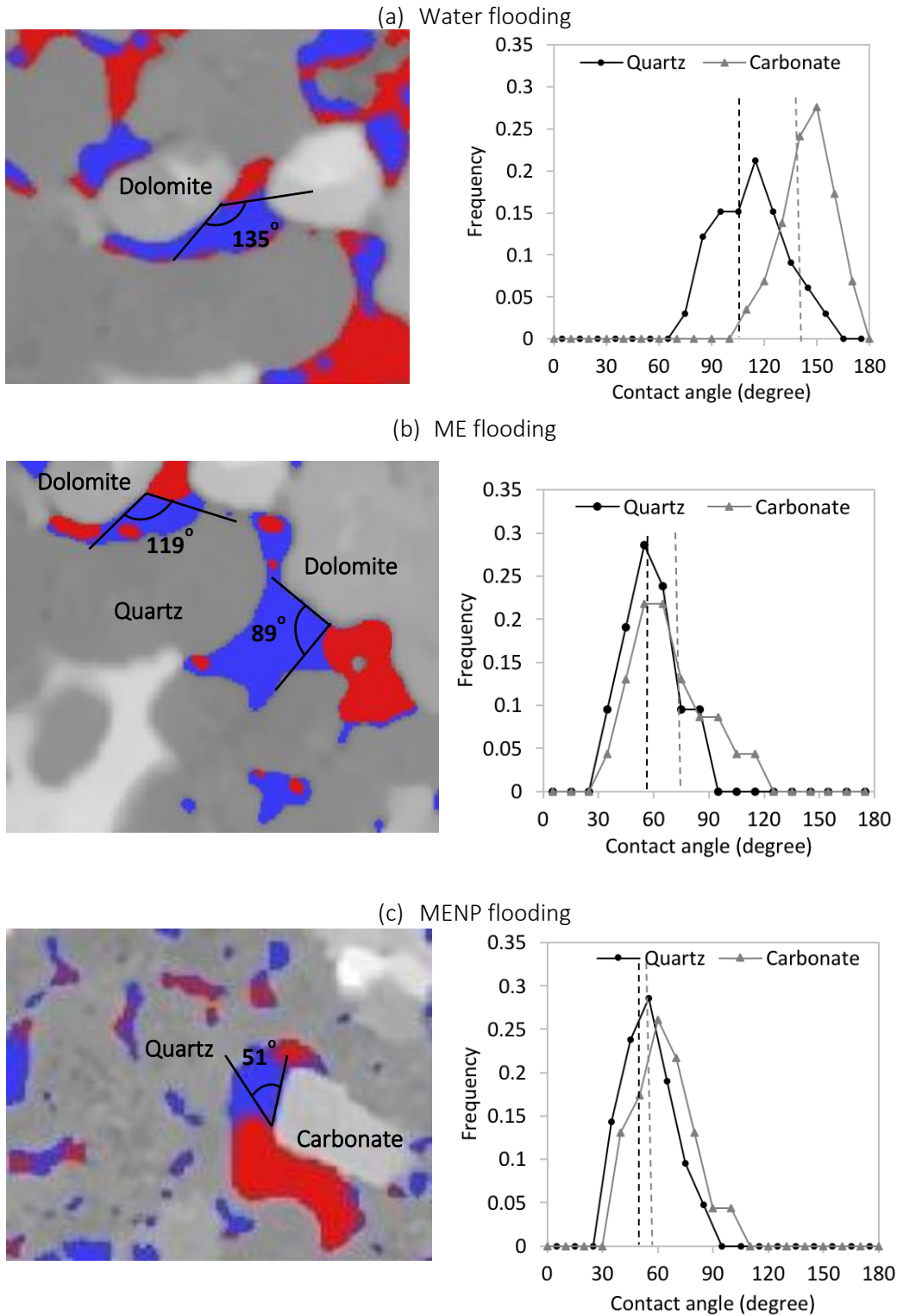
Figure 6. *In-situ* contact angle distribution at oil/brine/minerals contact line at the end of (a) water flooding, (b) ME flooding, (c) MENP flooding. Examples of image analysis are given for carbonate (especially dolomite cement) where oil is in red, brine is in blue, and remaining colors represent different minerals in the rock.
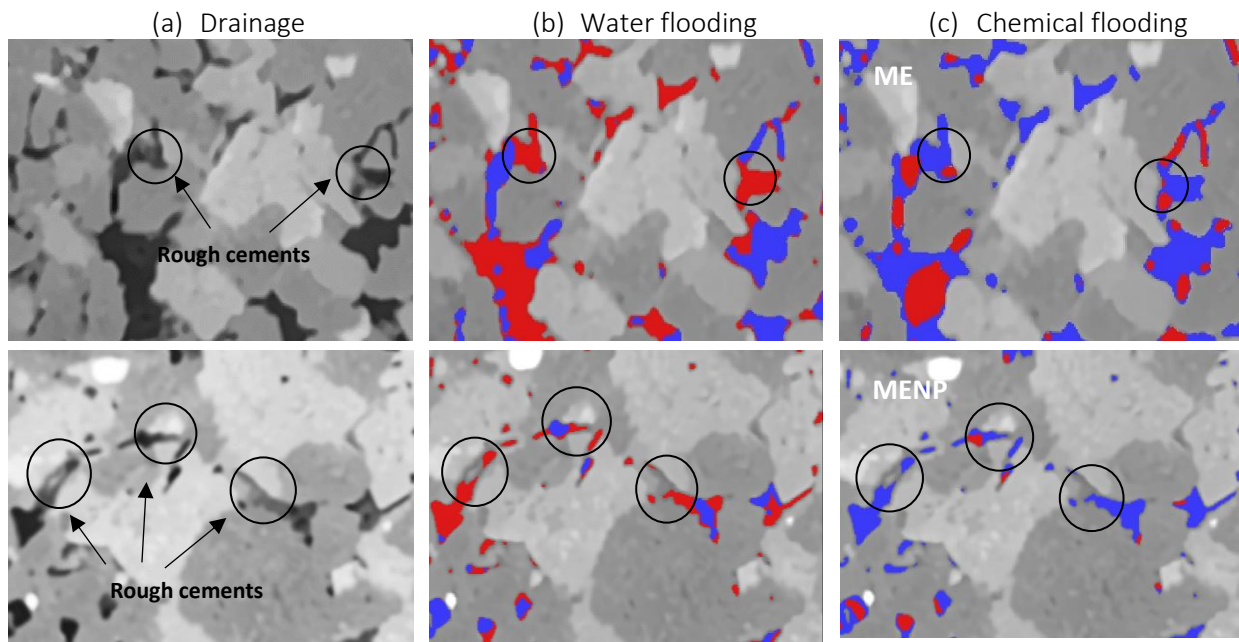
Figure 7. 2D cross-sections of pore space: (a) dry sample, (b) after water flooding, and (c) after ME or MENP flooding. Brine and NAPL are shown in blue and red, respectively. The field of view area is about 0.55 x 0.40 mm^2.
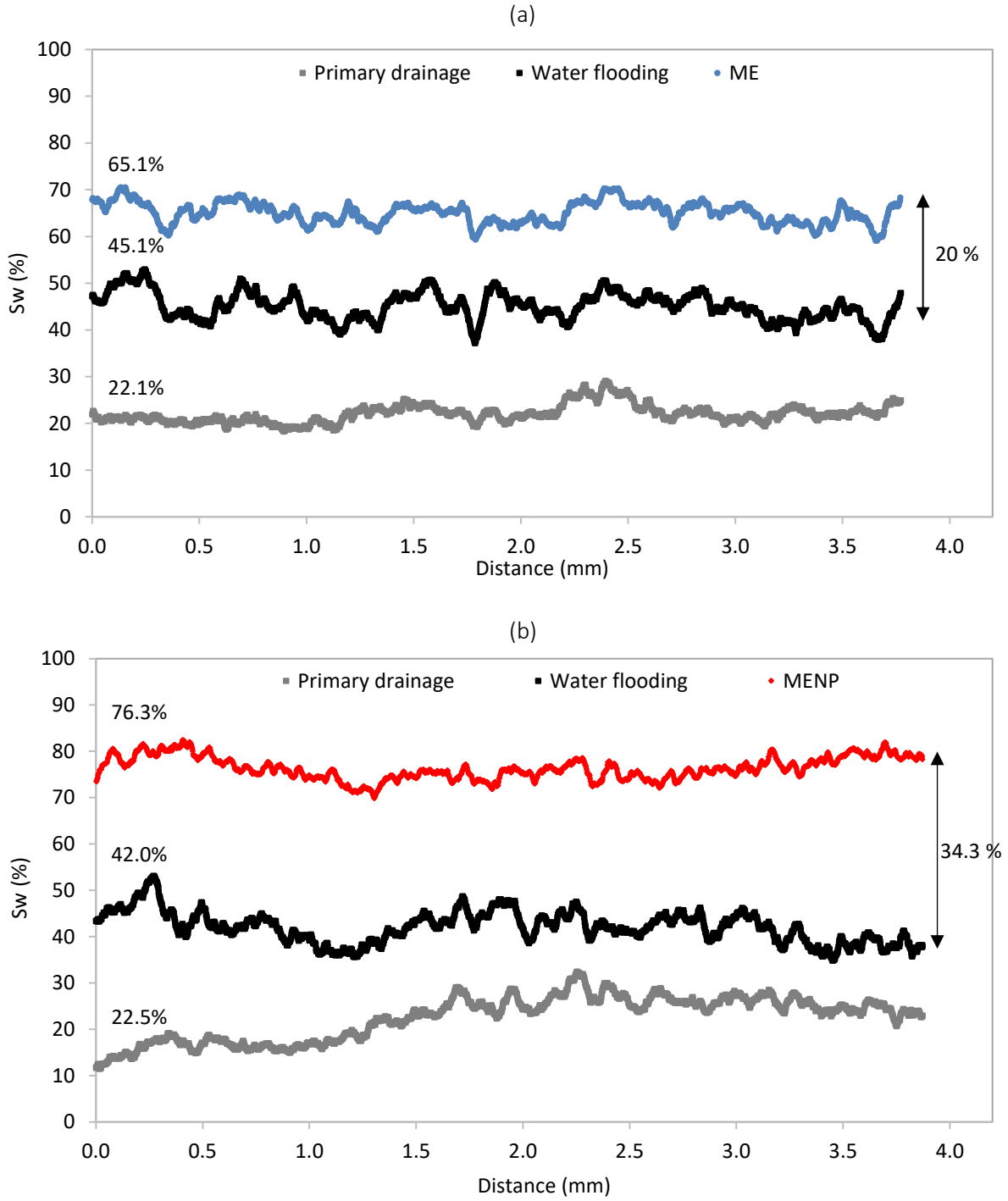
.

Figure 8. Saturation profiles at the end of flooding processes (a) ME flooding, (b) MENP flooding.